Improving the Amount of Captured Energy of a Point-Absorber WEC on the Mexican Coast

Alejandro Martinez Flores [1], Ayrton Alfonso Medina Rodríguez [2], Edgar Mendoza [1,*] and Rodolfo Silva [1]

1 Institute of Engineering, National Autonomous University of Mexico, Circuito Escolar, Mexico City 04510, Mexico; alexander_mtz_flores@hotmail.com (A.M.F.); rsilvac@iingen.unam.mx (R.S.)
2 Department of Ocean and Resources Engineering, School of Ocean and Earth Science and Technology, University of Hawaii at Manoa, 2540 Dole Street, Holmes Hall 402, Honolulu, HI 96822, USA; ayrtonamedinar@gmail.com
* Correspondence: emendozab@iingen.unam.mx

Abstract: Although there are constant improvements in wave energy converter (WEC) technology, it is crucial to investigate site-specific sea conditions for optimal power absorption and efficiency. This study compares the efficiency of a floating buoy-type WEC device, with three differently shaped floats: a semi-sphere, a cylinder considered suitable for a location near Ensenada, on the Baja California peninsula, and a novel, rounded, semi-rectangular float. A statistical analysis of the wave climate of the last 42 years was performed to define the conditions to which the device is subjected. The WEC location was chosen for shallow waters, using a computational model that solves the modified mild slope equation. The hydrodynamic response of the three float designs was then analyzed in the frequency and time domains, using the software ANSYS AQWA 19.2, to assess the dynamics of the floating body, the forces exerted, and the power absorbed, as well as the suitability of the proposed power take-off (PTO) system. The findings show that the proposed float design absorbs the most energy, with an annual power of 135.11 MW, and that the PTO mechanism is appropriate.

Keywords: wave energy converter; floating buoy; mild slope equation; hydrodynamic response; energy absorption; WEC efficiency; captured energy

1. Introduction

To meet the constantly increasing demand for electricity, a transition from fossil fuel energy systems to renewable energy technologies is required. The Paris Agreement of 2016, signed by over 126 countries and regions, makes commitments to improving resilience to climate change and reducing greenhouse gas emissions [1]. Renewable energy technologies are being developed to take advantage of a range of clean energy sources, with marine renewable energy (MRE) a plentiful and promising resource for achieving this goal [2].

The principal sources of MRE are thermal gradient, waves, tidal/currents, and salinity gradient, which cover 53%, 36%, 9%, and 2%, respectively, of the worldwide marine energy installed capacity [3,4]. Neil and Hashemi [5] estimated that the use of ocean renewables will consistently increase, and they will contribute 748 GW to the global energy supply by 2050. Wave energy is one of the densest marine energy sources per area unit [6]. It can be harnessed on a large scale since the infrastructure required is moderate in size, and it is possible to share the costs of installation and maintenance with marine structures already in existence. In this way, wave energy could become more economically profitable than other MRE sources [7].

On a worldwide scale, potential wave energy is estimated to be about 29,500 TWh per year [8] and each wavefront is considered potentially able to transmit an average of 10–15 kW/m [9,10]. Like most of the planet's resources, wave energy is distributed unevenly; areas subject to regular winds have the greatest energy potential, so the extra-tropical regions (30–60°) have the most wave power, over 60 kW/m, and this decreases

towards the equatorial regions to less than 10 kW/m [11]. On the Mexican coasts, the focus of this study, wave energy is very variable; in the Gulf of Mexico, it is less than 10 kW/m, while in the Pacific, it is 10–20 kW/m [12], with the greatest power availability being in the western part of the Baja California peninsula at 21 kW/m [13].

In recent years, a wide variety of wave energy converters (WECs) have been designed and prototyped [14]. WECs can be classified based on their location [15] (onshore, nearshore, offshore), size and orientation with respect to the incoming wave [16], the working principle [17] (pressure differential WECs [18], overtopping WECs [19], floating WECs [20]), power take-off system, (air turbines [21], hydraulic systems [22], linear generators [23], and mechanic [24]). Some of the most well-known examples of these technologies are the Oscillating Water Column (OWC) device (LIMPET [25], Sakata [26], REWEC3 [27], Mutriku [28], and Mighty Whale [29]); overtopping devices (TAPCHAN [30] and Wave Dragon [31]); and oscillating bodies (IPS buoy [32], AquaBuoy [33], Pelamis [34], SEAREV [35], AWS [36] and Oyster [37]).

For all of these devices, the accompanying literature explains how the cost of manufacture, installation, and maintenance rises as it becomes bigger. The design process seeks to optimize all the components of the device in order to produce an economically feasible system. To date, one of the most promising WEC designs is the point absorber (PA). This comprises a floating body, with relatively small dimensions compared to the incident wavelength, and a support system that attaches it to the sea bottom. The kinetic energy of the heave motion produced from the interaction between the wave and the floating device is absorbed by a power take-off (PTO) system, that converts this mechanical power into electrical power. Examples of PA-WECs include the Wavestar [38], SeaBased [39], Wavebob [40], and Aquabuoy [41].

Researchers have worked for decades to improve the amount of extracted power from PA-WECs using analytical, numerical, and experimental approaches. Early work by Budal and Falnes [42] was developed by Goggins et al. [43], who presented a methodology to optimize the structural geometric configuration of a floating WEC, taking into consideration the average annual wave energy spectrum of the location for which it was designed. Shi et al. [44] analyzed the design of a conical-bottom WEC with a PTO system. McCabe [45] presented a systematic method of optimizing the shape and size of a WEC to improve its capture efficiency using a genetic algorithm. Their system oscillates in the range of the prevailing wave frequencies, to produce maximum motion and, therefore, power [46].

Huang et al. [47] developed a framework to study how fluids and structures interact using computer simulations (Computational Fluid Dynamics, or CFD) and a method called finite element analysis. They looked at how flows of fluid that cannot be compressed behave in three dimensions, over time, using a specific mathematical approach (the Navier–Stokes equations) and a technique called the finite volume method. Devolder et al. [48] used a CFD software called OpenFOAM version 3.0.1 to simulate how a group of WECs behave in a model of a wave tank, looking at how the water and the structures affect each other. Zhang et al. [49] studied a floating WEC that is anchored by chains, using Reynolds–Averaged Navier–Stokes (RANS) equations and the k-ω turbulence model. They used advanced mathematical equations to show how the device interacts with water movement. Zou and Abdelkhalik [50] set up a CFD simulation to study a WEC that can change shape, using a specialized tool for understanding how fluids and structures interact with ANSYS and fluid–structure interaction tool. Huang et al. [51] focused on using AQWA for the hydrodynamic analysis and simulation of Pelamis-like wave energy converters, comparing different simulation methods such as the linear damping model and the Coulomb torque model with a hydraulic Power Take-Off (PTO) mode. Pastor and Liu [52] analyzed and optimized the power absorption of a WEC using ANSYS AQWA 19.2.

While there are many works on the optimization of a PA WEC device, these are all site-specific, and their findings may not be applicable elsewhere. This work seeks to assess the performance of a floating-type PA-WEC, with three distinct forms, off the coast of Ensenada, Baja California, Mexico, a location with high potential for the successful deployment of

WEC technology. The behavior of the device was numerically simulated in the frequency and time domains from which the extractive capacity of each buoy and the response of a proposed mechanical PTO were quantified.

2. Materials and Methods

2.1. Problem Definition

The WEC device analyzed in this work is classified as a floating buoy type. Figure 1a,b show the plan and side views of the proposed WEC model.
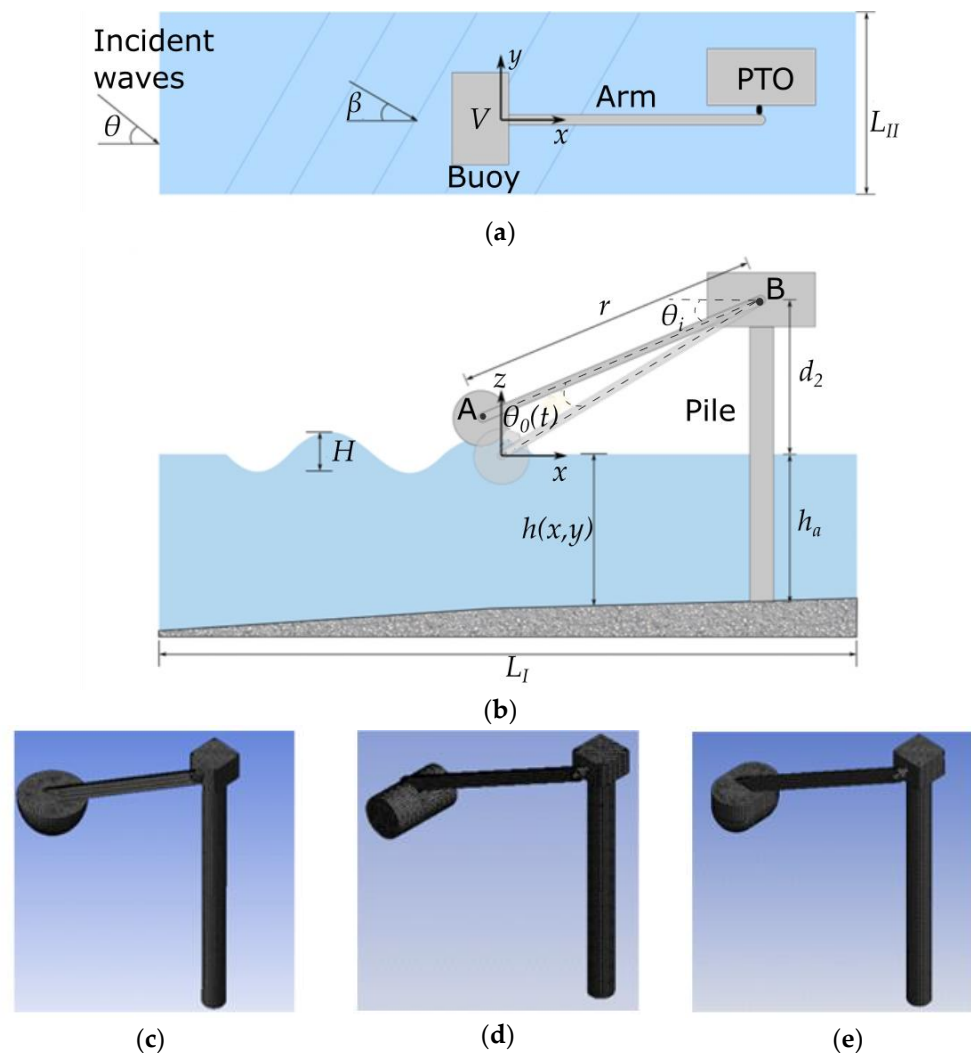
Figure 1. (**a**) plan and (**b**) side views of the PA WEC with the three distinct floats analyzed: (**c**) the semi-sphere, (**d**) the cylinder, and (**e**) the proposed design.

It was assumed that the sea bottom is impermeable with a length of L_I, and width of L_{II}. The waves were considered to propagate from left to right, with a height of H, and an incident angle of θ. The water depth $h(x,y)$ is considered uneven. In the reference coordinate system, the x-axis is positive to the right, while the z-axis is positive upwards. The origin of the reference system is located at the center of gravity of the buoy in static equilibrium.

The WEC of volume, V, is coupled to a lever arm whose length is $r = AB$, which activates a mechanism known as the power take-off (PTO) system. This is at a height d_2 above the mean sea level (MSL). The device is anchored to the sea bottom at a depth of h_a. The angle formed between the lever arm and the upper surface of the float is θ_i. The interaction effects of the waves with the buoy produce an angular degree of freedom, $\theta_0(t)$,

that is time-dependent and is considered relative to the initial conditions of the system. Finally, the buoy and the diffracted incident wave interaction form the angle β.

2.2. Maritime Climate

From the wave data of the European Centre for Medium-Range Weather Forecasts Re-Analysis version 5 (ERA5) for the period between 1979–2021, it was found that the Pacific Coast of the Baja California peninsula has the greatest wave energy in Mexico (Figure 2). This ERA5 dataset provides hourly data on significant wave height, mean period, and wave direction. The time series analysis shows that the wave direction extends 52% from WNW, as seen in Figure 2c. The ERA5 point nearest to Ensenada is at 117.0° W, 32.0° N, Figure 2a.
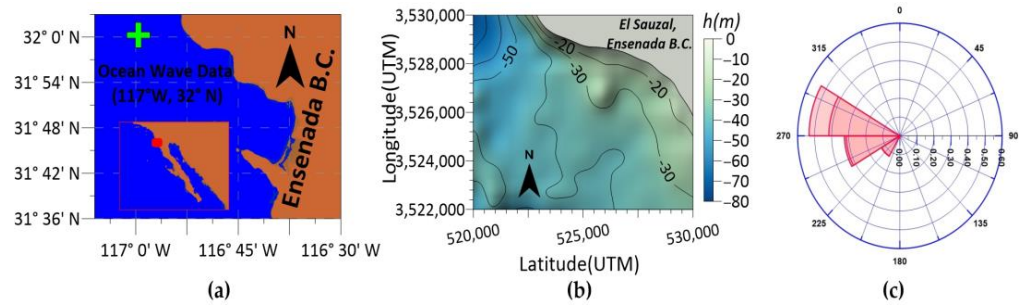
Figure 2. (**a**) Location of the study site and the wave data point; (**b**) bathymetry of the study area near Sauzal, in the municipality of Ensenada, Baja California, Mexico; and (**c**) the annual wave rose.

The values of the significant wave height, H_s, and mean period, T_m, in the four seasons of the year and annually, are shown in Table 1. It can be seen that the winter has the greatest H_s and T_m, indicating that the waves are more energetic in this period.

The wave conditions for the Ensenada coast are presented in Figure 3, in terms of their annual joint probability distribution (JPD). There is a predominance of mean periods of 9–11 s, whereas for H_s the most frequent values are 1.0 and 1.5 m, with 25.6% occurrence. Most wave heights are between 0.5 and 2.5 m, with only 1.5% of waves exceeding 3 m in height. The predominant waves have frequencies of 7–13 s with a 94.8% occurrence.
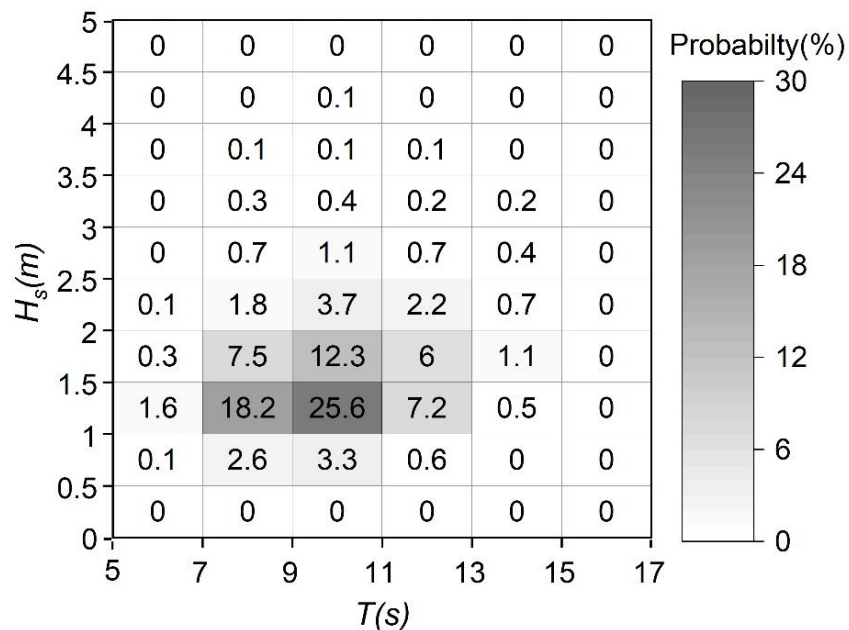
Figure 3. Joint probability distribution (%) for the ERA5 point nearest to Ensenada (117° W, 32° N).

Table 1. Values of the waves in each season of the year and annually.

	Annual		Spring		Summer		Autumn		Winter	
%	H_s	T_m	H_s	T_m	H_s	T_m	H_s	T_m	H_s	T_m
50	1.85	10.10	1.82	9.45	1.44	9.32	1.89	10.49	2.17	10.92
33.33	2.04	10.27	1.97	9.47	1.51	9.41	2.08	10.58	2.40	11.03
10	2.60	10.55	2.41	9.52	1.70	9.74	2.64	10.65	3.05	11.20
1	3.72	10.86	3.29	9.46	2.07	10.68	3.69	10.72	4.26	11.38

Figure 4 shows the probability and the wave energy in terms of wave heights and periods.
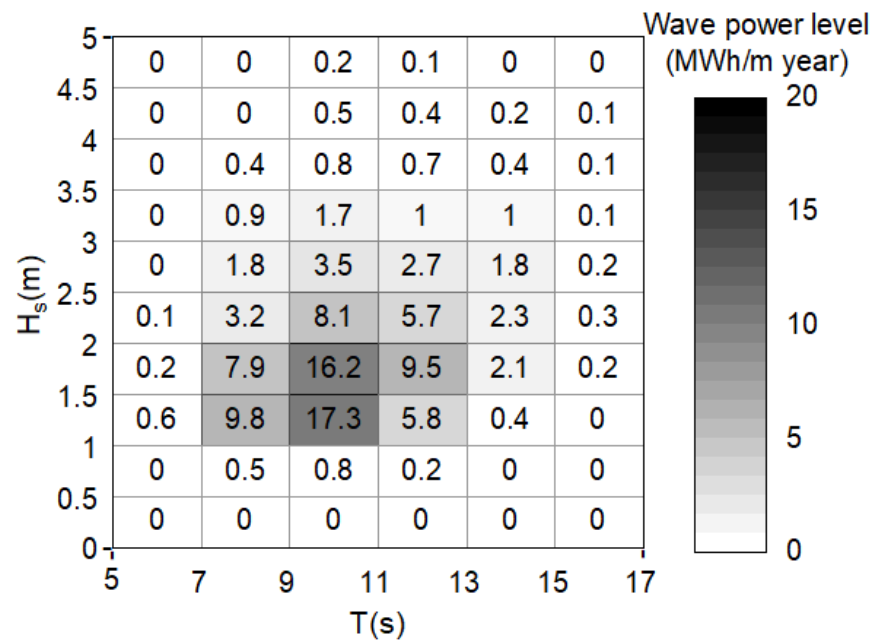
Figure 4. Combined scatter and energy diagram: the colors denote the annual wave power (MWh/m year), and the numbers indicate the occurrence probability per year (%) in terms of significant wave height and peak period.

The most likely wave periods range from 7 to 13 s, with wave heights H_s ranging from 1–3 m, generating powers over 1.7 MWh/m per year. The most energetic conditions are found between periods 9 and 11 s, with a H_s of 1–2 m, and a maximum of 17.3 MWh/m per year. The energy per unit area averaged in a wave period, E, can be computed directly from the hindcast data as follows [53]:

$$E = \rho g H_s^2 / 16 \tag{1}$$

where ρ is the density of the fluid and g is the acceleration due to gravity. On the other hand, the wave power level, P, per unit width can be given as follows:

$$P = \rho g^2 H_s^2 T_e / (64\,\pi) \tag{2}$$

with T_e representing the energy period. The measured sea states are often specified in terms of either the mean period or peak period (T_p). When the mean period T_m is known, one means of estimating T_e is as follows:

$$T_e = \alpha T_m \tag{3}$$

where the coefficient α depends on the frequency spectrum model, assumed to be equal to 1 [54].

Equation (2) is the deep-water approximation used in this study to describe the wave power for the nearshore region of Ensenada. By considering an average significant height H_s = 2.04 m and a wave energy period $T_e = T_m$ = 10.27 s, see Table 1, and applying Equation (2), the resultant wave power per unit width is approximately 20.84 kW/m.

2.3. Hydrodynamics of the System

The initial hydrodynamic modeling of WECs usually assumes that the hydrodynamic forces of the float are those obtained from linear diffraction theory, i.e., viscous effects are ignored and only potential forces are considered. The response of a single floating body is, therefore, generally described using a mass-spring system. Assuming a 6-degree-of-freedom linear system, the motion equations for this analysis can be represented as:

$$\sum_{j=1}^{6} \left(M_{kj} + A_{kj}\right)\ddot{x}_j + B_{kj}\dot{x}_j + C_{kj}x_j = F_k \quad k = 1, 2, \ldots, 6 \tag{4}$$

where k and j denote the hydrodynamic properties in the k-mode because of the motion in the j-mode; M_{kj} is the mass of the structure; A_{kj}, B_{kj}, and C_{kj} are the added mass, damping, and hydrostatic restoring matrices, respectively; and F_k represents the other external forces in the k_{th} mode. A detailed discussion of linear diffraction theory is found in Newman [55].

The primary mechanism of the proposed PA for energy extraction is the heave motion; so, at this stage, only this motion of the float is considered, and the motion equation is given by:

$$(M + A_{33})\ddot{x}_3 + B_{33}\dot{x}_3 + C_{33}x_3 = F_3(t) \tag{5}$$

where M is the mass of the system; A_{33}, B_{33}, and C_{33} are the added mass, damping, and hydrostatic matrices, respectively, in the heave direction; and F_3 is the external force on the body in the heave direction. It is worth remembering that, in addition to wave excitation and mooring forces, external forces may include other forces, such as mechanical forces (e.g., PTO forces).

2.4. The PTO Mechanism

As seen in Figure 1, The heaving movement of the floating buoy drives the vertical, rise and fall, movement of arm r at a low speed. At higher speeds, a rotational movement is produced in the PTO mechanism, composed of a unidirectional gearbox and a flywheel, and electricity is generated from arm B to three unidirectional clutches (UC), a gear train to multiply speed (MG), a flywheel (FW), and an electric generator (G) as seen in Figure 5.
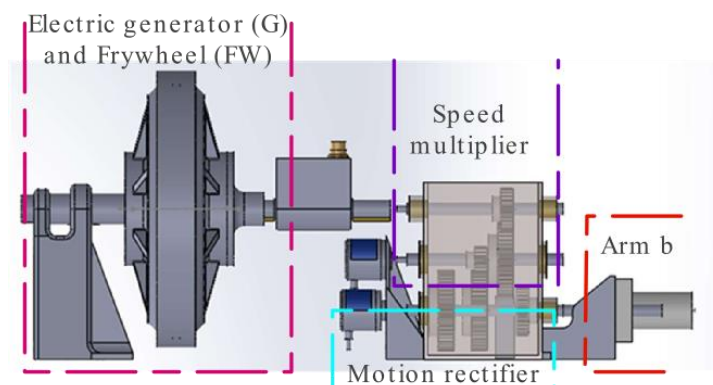
Figure 5. Side view of the PTO mechanism.

The design is based on a mechanism that increases the speed ratio to 1:2. In addition, it fully rectifies the movement, by making use of the rise and fall of the float through arm r, with two unidirectional clutch bearings, UC1 and UC2, located, respectively, inside gears N1 and N5, as well as gears N2, N3, and N4 and shafts 1, 2, and 3, seen in Figure 6a.

UCs are used since they take advantage of rotation in one direction only. To be more specific, as the float rises, arm *r* connects with shaft 1 (E1), activates by UC1, turning gear N1 in a clockwise direction. This then drives shaft 2 (E2) through gears N2 and N3 which in turn moves N4 and N5, respectively, thus deactivating UC2 so that it does not transmit power, allowing the float to take advantage of the upward movement.
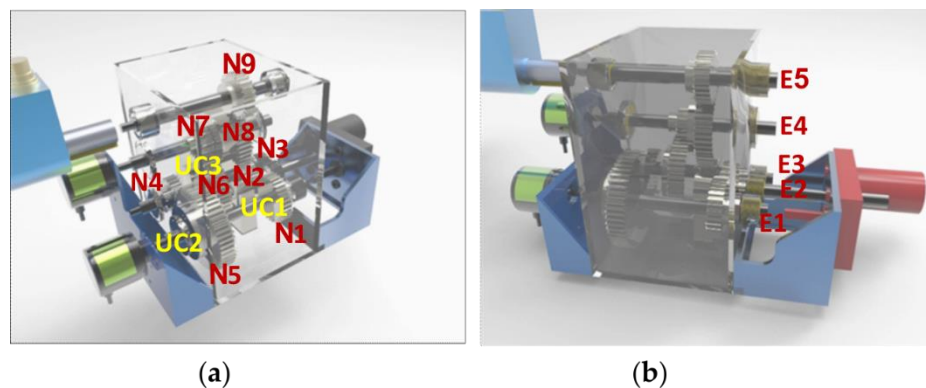
Figure 6. (**a**) Arrangement of gear elements (N1 to N9) and unidirectional clutch bearings (UC1 to UC3) and (**b**) location of the axles (E1 to E5).

When the float falls, the energy is sent to E1, which rotates counter-clockwise, engaging UC2. N5 transmits this power to E2, through N4, causing UC1 to detach and N1 will not transmit power. In this way, the reciprocating movement of the E1 input is corrected to a unidirectional clockwise movement in E2, which acts as the input to the multiply gear (MG).

Once the rotation is restricted to one direction, the rotations for the generator must be multiplied, which is why the operation of the box is verified, and an arrangement of gears from E2 to the generator with gears N6, N7, N8, and N9 with a 1:5 ratio. Therefore, from E1 to the generator, there is a speed ratio (R_v) of 1:10. Another clutch bearing, UC3, is installed in gear 6 to keep the inertia flywheel at a more consistent speed for the generator, and to decouple it from the transmission when the input speed is low.

It should be emphasized that the optimum ratio for the stage of multiplying the revolutions has not yet been established; this will depend on the site-specific wave conditions, the power to be obtained, and the generator.

Furthermore, a flywheel is installed within MG, which is essentially a mechanical energy storage device on axle 5 (E5) in conjunction with N9 whose function is to maintain a more constant speed in the electrical generator G. According to the rationale, when the float reaches its lowest position on the vertical axis, it begins to rise at a speed equal to zero, with maximum acceleration until it reaches a point higher where the same conditions are met and begins its fall again, to return to the lowest point. The speeds and accelerations fluctuate spatially and temporally as the float moves up and down, which is transmitted to the E1 where the angular speed is not constant due to the changing motions of the float; for this reason, the flywheel (FW) is used. Figure 6 shows a profile view of the mechanism.

WECs such as the Wavestar and Eco Wave Power have similar systems to that described here. Their operation principle is based on floats that move articulated oscillating arms, but their PTO systems are more complex and, thus, more expensive. These are based on sliding pistons, hydraulic systems, or linear generators, whereas the proposed device here does not transform the energy into an intermediate pneumatic or hydraulic power stage.

PTO Dynamics

The PTO amplifies the system movement with a speed ratio, R_v. In this study, three cases were compared, first, with no clutch bearing, then, with two clutch bearings, and

finally, with three clutch bearings and a flywheel. Once the angular displacement, $\theta_0(t)$, at the PTO input is known, the dynamics can be analyzed for each case. Equations (6)–(9) show how each velocity and position are determined

$$\omega_0 = \dot{\theta}_0(t), \tag{6}$$

$$\omega_1 = \dot{\theta}_1(t) \text{ and } \theta_1 = R_V \theta_0(t), \tag{7}$$

$$\omega_2 = \left| \dot{\theta}_1(t) \right| \text{ and } \theta_2 = \int_0^t \omega_2 dt \tag{8}$$

$$\omega_3 = \max\left(\omega_{max(j),2} + \alpha t, \omega_2\right) \text{ and } \theta_3 = \int_0^t \omega_3 dt, \tag{9}$$

where ω and θ, correspond to the speed and temporal position, respectively. The subscripts 0, 1, 2, and 3 indicate the entrance to the PTO, the first, second, and third cases analyzed, respectively. The term α is the flywheel angular acceleration, t is the time, $\omega_{max(j),2}$ is the local maximum speed of ω_2, and j indicates the corresponding maximum value.

2.5. WEC Modeling

For the WEC shown in Figure 1, it was necessary to create a computer model representation of the device. There are different means to define the device geometry [56]. In this paper, a solid model approach was chosen using SolidWorks 2018. Three types of floats were analyzed: a semi-sphere, a horizontal cylinder, and, the new design, a rounded semi-rectangle which is referred to from here as the proposed design. The PTO and the pile are considered as one body. Each of the three floats has a width of 3 m and a volume of $V = 7.06 \text{ m}^3$, with the following dimensions: $r = 10$ m, $d_2 = 5.5$ m, $h_a = 5$ m, $\theta = 30°$, and $\beta = 0°$.

It should be mentioned that the value of h_a was selected to reduce the computational domain. The pile was circular, with a diameter of 1 m, and with a concrete density of 2400 kg/m^3. Both the float and the arm were considered to have a uniform density of 470 kg/m^3. Figure 7 shows the dimensions of each element involved.

The buoy and the arm are joined and treated as one element, as are the pile and the PTO. Using SolidWorks, the physical properties of the float were obtained: the center of gravity, the moment of inertia, volume, surface, and weight.

The origin of coordinates x and y is at the center of the mass of the semi-sphere float in initial conditions while the z-axis is at the mean water level. The physical properties of the semi-sphere-arm, cylinder-arm, proposed float-arm, and pile-PTO are described in Table 2.

To analyze the behavior of the WEC in the frequency domain, the Hydrodynamic Diffraction module of ANSYS AQUA was used. To carry out this type of simulation, the properties of the mass of the bodies were configured in the center of gravity of each body.

Appendix A shows the maximum *RAO* for the movement of the heave in the frequency domain with respect to the number of mesh nodes for each scenario analyzed. According to the mesh independence study, the number of nodes was taken when the relative percentage error was less than 1%; thus, the numerical model mesh had a maximum element size of 0.2 m, with 6220, 6109, and 5982 nodes for the hemisphere, cylinder, and proposed geometry, respectively.

Figure 1c–e shows the numerical mesh for each float analyzed. The supporting pile was defined as a fixed structure, and the connection between the PTO and the arm was configured as a hinge so that the arm could rotate around the connection point coordinates 8.6, 0.0, and 5.5 m. Because it is dependent on the operation of the system, the arm-buoy was described as a free-moving body. The frequency domain was configured in an interval of 0.05–0.5 Hz, $\beta = 0°$; the depth and wave conditions, Table 1, were determined from the data for the study area.

The three floats. Units are in m	
Semi sphere	**Cylinder**

Proposed design	**Arm**
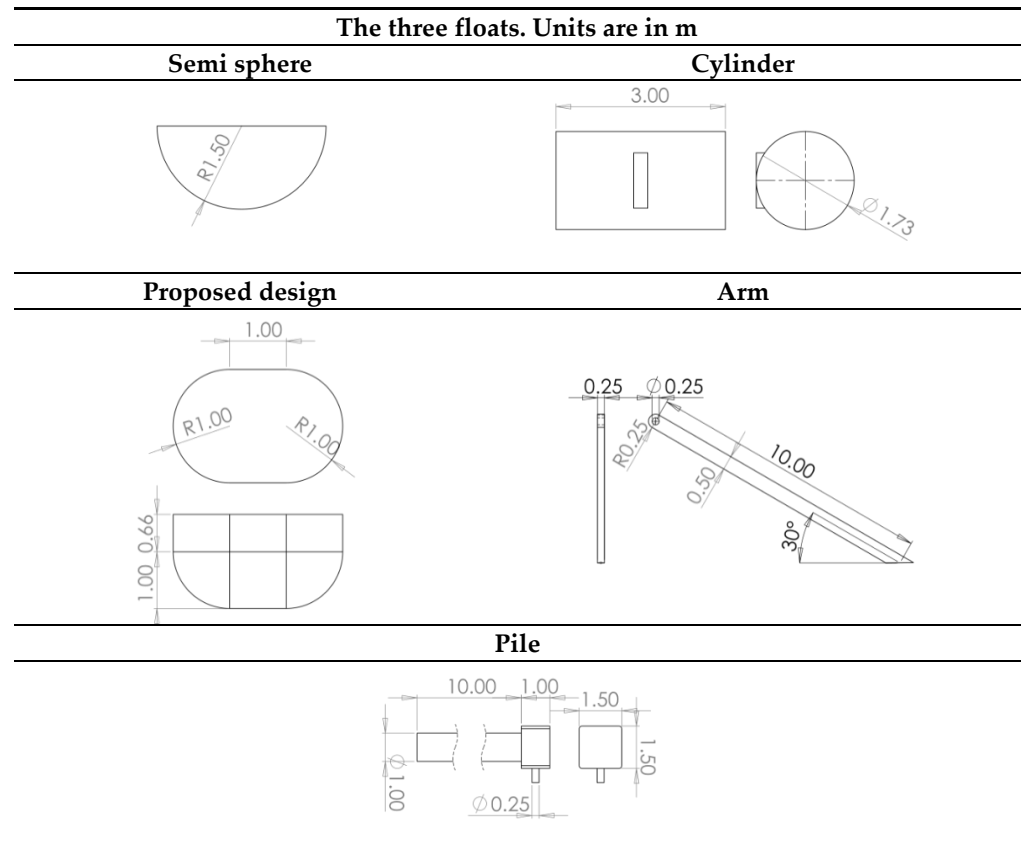
Pile

Figure 7. Dimensions of each part of the wave energy converter (WEC).

Table 2. Geometry of the semi-sphere-arm, cylinder-arm, proposed float-arm, and pile-PTO.

	Geometry			
Parameter	**Semi Sphere-Arm**	**Cylinder-Arm**	**Proposed Float-Arm**	**Pile-PTO**
Volume [m^3]	8.32	8.34	8.31	10.11
Mass [kg]	3914	3920	3910	24,287
Surface area [m^2]	36.92	36.9	35.74	42.11
Centre of gravity[m]				
x-axis	−0.657	0.653	0.701	8.59
y-axis	0.0	0.0	0.0	1.12
z-axis	0.752	0.443	0.411	1.34
Moment of inertia [kg/m^2]				
I_{xx}	10,450	10,511	9574	386,335
I_{yy}	25,353	24,156	23,951	2,149,103
I_{zz}	17,899	18,635	18,035	1,828,260

3. Results

3.1. Study Area

As mentioned previously, the wave data were obtained for deep water, 32.5 km from the community of Sauzal, in the municipality of Ensenada (116°41′4.22″ W, 31°52′59.72″ N). For this reason, it is convenient to numerically propagate the wave from this location to the area of interest. Therefore, the domain was reduced to that shown in Figure 2b, which was 8 × 10 km, and the WAPO (WAve Propagation On the Coast) numerical model was used. This tool propagates a monochromatic wave train over a variable sea bottom [57], preferably

in shallow and intermediate waters, and solves the modified mild slope equation in its elliptic shape. The WAPO model has been successfully used in studies in which various types of structures (e.g., breakwaters, WECs, etc.) [58–60] are located in intermediate and shallow water (in this case they were modeled at 30 m water depth). This model can reproduce wave phenomena such as shoaling, refraction, diffraction, reflection, and the dissipation of energy induced by bottom friction and wave breaking [61].

When locating a WEC, it is best placed close to the coast and in shallow waters where there is high wave energy. The numerical input conditions were collected from the annual statistical analysis: H_s = 2.03 m, T_m = 10.27 s, with a WNW direction ($-11.25°$ with respect to the west). A non-reflective beach and a grid of 1001×801 nodes were used. Figure 8a,b show the results obtained for the wave height and the wave power level, respectively. The UTM coordinates (526,000 E, 3,256,000 N) were selected to analyze the mechanical performance of the device in a water depth of 30 m, wave height of 2.2 m, and wave power of 24.5 kW, which is a highly energetic area.
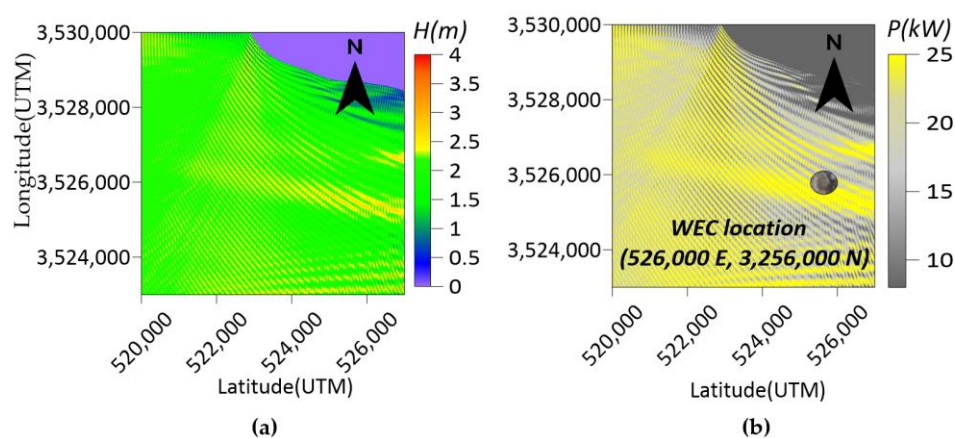
Figure 8. Maps of (**a**) wave height and (**b**) wave power.

3.2. Frequency-Domain Analysis

Figure 9 shows the numerical results obtained with ANSYS AQUA 19.2 for the three floats analyzed. Figure 9a shows the variation of the added mass with respect to the analyzed frequency of 0.05–0.5 Hz, with a constant bathymetry of h_a = 30 m. It is seen that the values for the three floats for the heave and surge movements reach a maximum value and then decrease as the wave period increases. For the heave motion, the maximum value for the semi-sphere was 5955 kg/m at ω = 0.107 Hz, followed by the cylinder: 4476 kg/m with ω = 0.054 Hz, and, finally, the proposed design: 4170 kg/m with ω = 0.057 Hz. The added mass is an additional force that resists the heave and surge movement; the optimum outcome would be that this be as low as possible. It can be observed that the proposed float has the least resistance to that movement. Figure 9a also shows that for this motion, high frequencies may give better performances from all three float designs.

Figure 9b represents the variation of the excitation force throughout the frequency; as the frequency decreases, the heave motion increases, while the surge decreases. In addition, the semi-sphere reaches values without significant changes from ω = 0.125 Hz, while the other two forms had similar hydrodynamic behavior. It is important to point out that this force is related to the amplitude of the wave; for this reason, it has units of N/m. It can be inferred that for high periods, the Froude–Krylov force is stronger, causing an increase in the vertical movement of the buoy and, as a result, in the angle within the x–y plane. This causes the translation speed to be greater than, or equal to, the electrical power generated.

Figure 9c illustrates the behavior of the hydrodynamic damping coefficient. It can be seen that the coefficients of the semi-sphere decrease as the wave period increases. As the wave period increases for the cylinder and proposed float design, the heave motion increases, to eventually reach a maximum at ω = 0.164 Hz, before decreasing again, whereas

the surge motion is almost the same for both. From this, it is clear that these devices are recommendable for long periods.
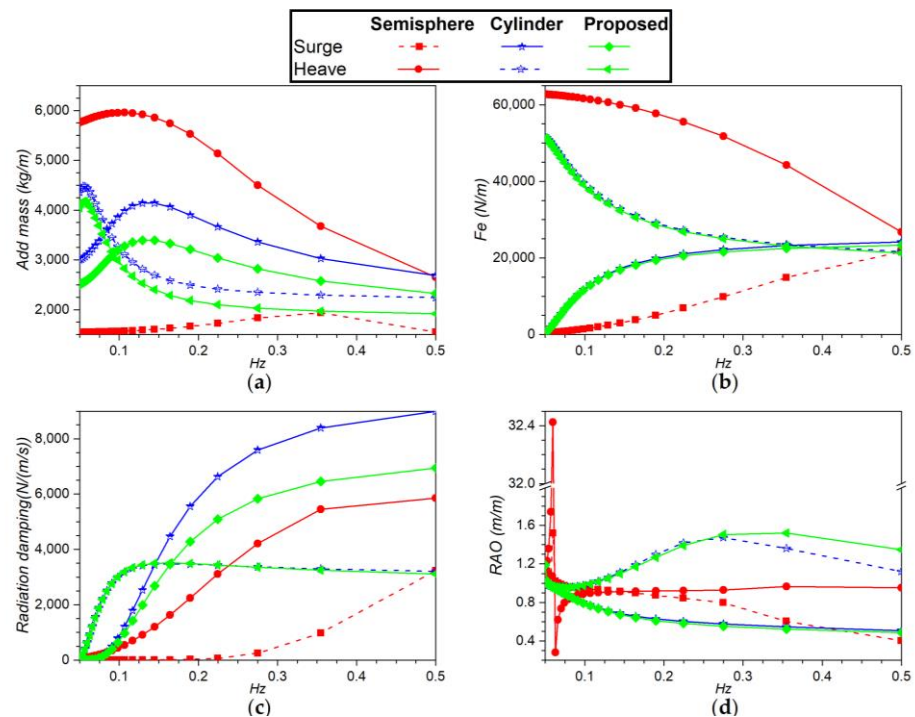
Figure 9. Frequency–domain analysis of the three bodies studied: (**a**) added mass, (**b**) excitation force, (**c**) radiation damping, and (**d**) response amplitude operator (RAO).

Finally, Figure 9d shows the response amplitude operator (RAO) of the float across the *z*-axis. It can be observed that the semi-sphere performs best with short wave periods, whilst the other two floats perform best with long periods. Point absorber WECs work best when the incident wave frequency matches their natural frequency, which is around 0.056–0.061 Hz for the semi-sphere, and 0.25–0.33 Hz for the other two float designs.

3.3. Analysis in the Time Domain

In this subsection, the findings of the hydrodynamic response in the time domain obtained by ANSYS AQWA 19.2 are provided. In these numerical simulations, a duration of 500 s was considered for the analysis and comparisons of the three float shapes. The wave conditions were set to H_s = 2.2 m, T = 10.27 s, and $\beta = 0°$. The first simulation allows analysis of the system behavior, under a second-order Stokes wave [62], with $F_{PTO} = 0$, a time step of Δt = 0.01 s, L_I = 50 m, and L_{II} = 50 m. From the displacement of the center of mass, it is possible to determine the angular displacement in the rotation axis *D*.

Figure 10a shows the temporal evolution of the angular motion transmitted to the PTO of the three forms over the entire simulation, whereas Figure 10b shows only the first 50 s of the simulation. It is seen that the angular displacement in the wave troughs and crests is greatest for the semi-sphere float, while the cylinder has the opposite tendency, and the movement of the proposed float design was between these two. Furthermore, for the three floats it can be seen that when there is a crest, there is more angular displacement than when there is a trough, as there is no damping effect from the water movement when ascending.

To determine the instantaneous power, Equations (10) and (11) are used with the data in Figure 10:

$$P = Fv \tag{10}$$

$$F = m(g + a) \tag{11}$$

where *P* is the power, *F* is the force of the body, *v* is the speed, *g* is the gravity, and *a* is the instantaneous acceleration.
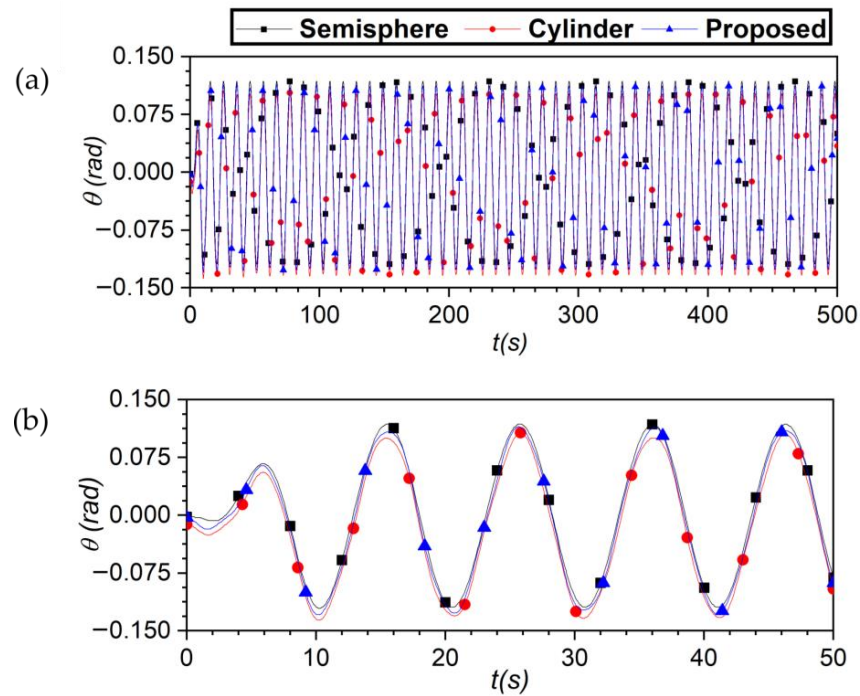
Figure 10. Angular displacement of the lever arm for the three floats was analyzed for (**a**) 500 s and (**b**) the first 50 s.

In Figure 11, the temporal evolution of the power absorbed over time is then obtained for the floats analyzed for the first 50 s. It can be seen that the absorbed power is variable over time, so it is necessary to determine a representative value. The average power achieved for the half sphere, cylinder, and proposed floats was 14.98 kW, 15.8 kW, and 16.87 kW, respectively.
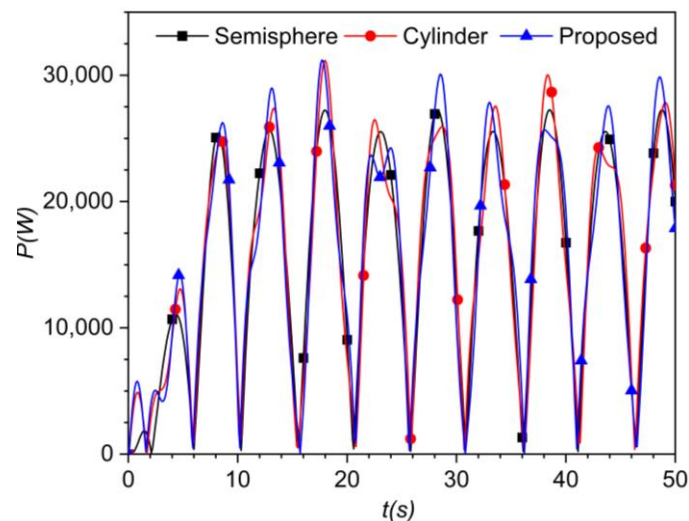
Figure 11. Instantaneous power against time for the three floats studied.

Figures 12 and 13 show the matrices of the average and maximum power, respectively, for the three floats analyzed. These figures show the periods from 5 to 15 s with different wave heights of between 0 and 4.5 m with $\beta = 0°$. For all three floats, for wave heights of less than 0.5 m, the absorbed energy is less than 4.11 and 8.7 kW for the mean and

maximum average power, respectively. The maximum power is found for periods of 5–7 s and wave heights of over 3 m. For the average power, the highest value is for the cylinder, with 90.68 kW, followed by the proposed float design, with 87.64 kW, and finally the semi-spheres with 71.81 kW. The maximum power follows the same order but with values of 437.7, 328, and 225.6 kW.
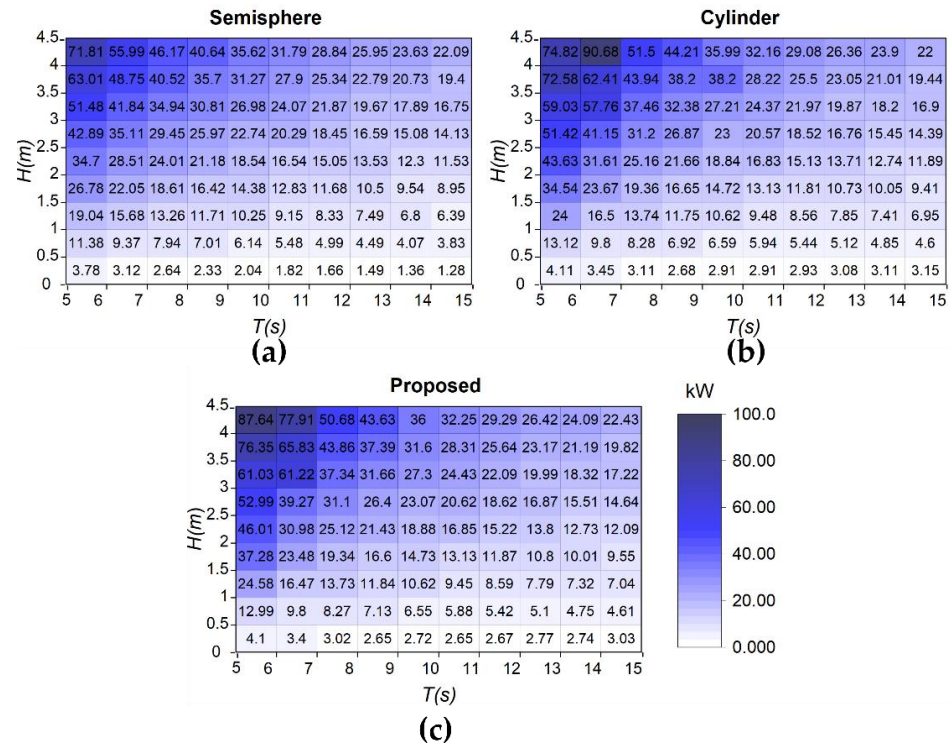
Figure 12. Average power matrices with variable wave periods and wave heights for (**a**) the semi-sphere, (**b**) the cylinder, and (**c**) the proposed design.

Table 3 compares the average power of each of the floats for various wave conditions. Firstly, for the significant wave height H_s, then for the average power matrix (Figure 12), and thirdly, for more frequently occurring wave conditions. It is seen that for the three cases, most power is absorbed with the proposed float design, followed by the cylinder. The average power for H_s with the proposed design is 10.88% greater than that of the semi-sphere. In the average power matrix, the proposed design increases 2.16 kW with respect to the semi-sphere, while for the average of the most recurrent conditions, the proposed design gives 1% and 2.71% more power than the semi-sphere and the cylinder, respectively.

Table 3. Comparison of the average power obtained by the three forms in various wave conditions.

	Float		
Condition	Semi Sphere	Cylinder	Proposed
H_s	14.98 kW	15.80 kW	16.87 kW
Average power matrix	19.85 kW	21.91 kW	22.01 kW
Average of the most recurrent conditions	15.06 kW	16.12 kW	16.16 kW
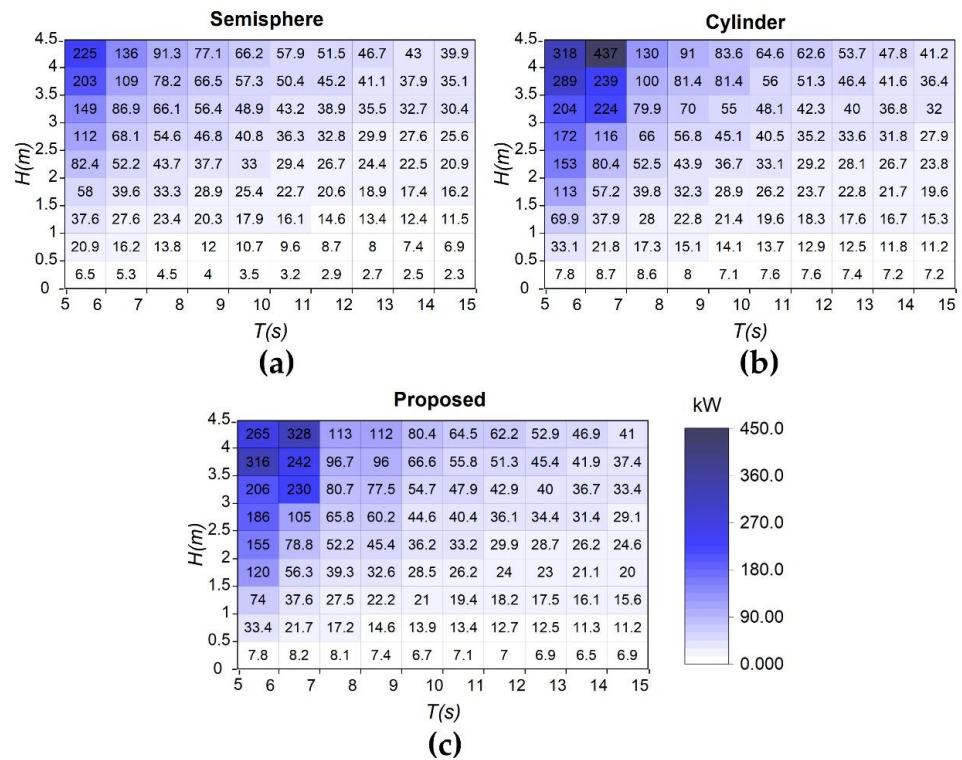
Figure 13. Maximum power matrices with different wave periods and wave heights for (**a**) the semi-sphere, (**b**) the cylinder, and (**c**) the proposed design.

Table 4 shows the seasonally significant wave heights, the associated wave periods, and the average power generated, in kWh, for each float analyzed (Figure 12). It is observed that the most energetic sea condition occurs in winter, followed by autumn, spring, and, finally, summer. However, the season with the highest power is autumn, followed by winter, and finally spring and summer with the lowest generation. The percentage differences between autumn and spring are 15.02%, 14.33%, and 14.39%, while for winter and spring, these are 4.65%, 2.78%, and 2.32% for the three floats, respectively. The table also shows the energy output for the year and that for the three floats. Most energy is harnessed by the proposed float design, followed by the cylinder, and lastly the semi-sphere. The same is true for the annual power generated by the devices, with a difference of 2.59 MW per year between the proposed float design and the semi-sphere.

Table 4. Average and generated power by season of the year and annual for the floats studied.

			Semi-Sphere		Cylinder		Proposed Float	
Season	Hs **(m)**	T **(s)**	**Avg. (kWh)**	**Generated (MW)**	**Avg. (kWh)**	**Generated (MW)**	**Avg. (kWh)**	**Generated (MW)**
Spring	1.97	9.47	14.38	31.57	14.72	32.32	14.73	32.34
Summer	1.51	9.41	14.38	31.57	14.72	32.32	14.73	32.34
Autunm	2.08	10.58	16.54	36.32	16.83	36.95	16.85	37.00
Winter	2.4	11.03	15.05	33.04	15.13	33.22	15.22	33.42
	Annual power (MW)			132.52		134.83		135.11

Once the dynamics of the PTO inputs are known (Figure 6), the transmission designed for the three floats is evaluated by applying Equations (6)–(9), with a speed ratio $R_V = 10$, $\alpha = -0.01$ rad/s^2 and the conditions of H_s at 33.33%, Table 1.

The results are shown in Figure 14, where only the first 50 s of the simulation are shown. The left column corresponds to the positions and the second column to the angular

velocities. These last two variables are compared with the output cases; the first output is without UC and is coupled, the second with two UCs and is also coupled, and the third is with three UCs and is uncoupled.

It can be seen that in the first case, only the gearbox works to increase the rotation speed, so that the PTO output is almost the same, but with amplified RV as much as the position and angular velocities oscillate. This could be a disadvantage, as the generator will have to constantly change the direction of the magnetic fields. One advantage of the second situation, when $\omega \geq 0$, is that ω will only be positive and the generator will always be moving in the same direction, causing the position to progressively increase. For the last case, a UC has a flywheel that absorbs movement in the form of kinetic energy which is employed so that when the PTO speed begins to decrease, the flywheel may be uncoupled, and the generator continues to work and does not exceed $\omega = 0$.
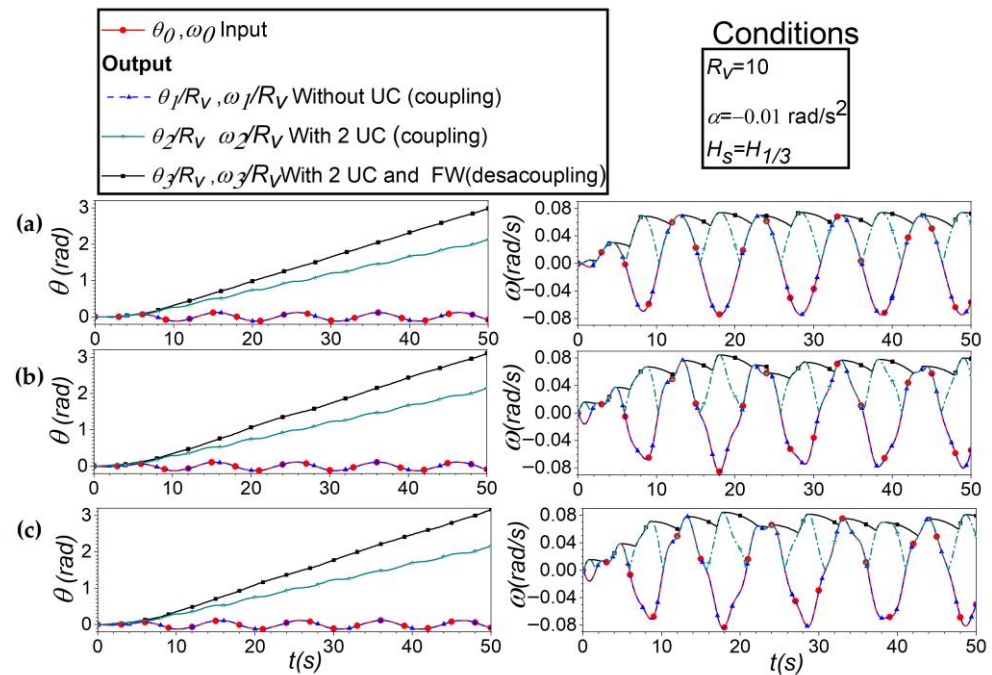
Figure 14. Angular positions and speed in the first 50 s from the PTO input and the cases analyzed at the transmission output: (**a**) semi-sphere, (**b**) cylinder, and (**c**) proposed float.

Therefore, the final proposal is examined in greater depth in this work, as this is the best choice for keeping the electric generator going, which translates into relatively constant electric energy. Further information can be found in [63]. Of the three floats examined, the first to reach its steady-state was the semi-sphere, at 20 s, then the proposed design, at 110 s, and finally the cylinder. In the transient stage, the velocities range between 0.054–0.076, 0.053–0.084, and 0.05–0.084 rad/s, while in the steady-state they range between 0.056–0.076, 0.052–0.074, and 0.053–0.077 rad/s, for the three float designs, respectively.

Figure 15 shows the matrix of the maximum angular displacement, at $T = 5$–15 s and H at 0–4.5 m, divided into intervals of 1 s and 0.5 m, respectively. The following trends are observed in the three cases: for small wave heights, of less than 0.5 m, the displacement is minimal regardless of the wave period, and as the height increases, the angle also increases. Furthermore, for $H > 1$ m it is observed that as the period increases, the movement is reduced, with the greatest displacement taking place when $H > 3$ m and $T = 5$–7 s. In this regard, the semi-spheres have the smallest displacement movement (0.017 rad) while the cylinder has the greatest (2.556 rad). In Figure 15a, which corresponds to the semi-sphere, the lowest values occur at $H < 0.5$ m, when $T > 7$ s, while the highest occurs at $H > 4$ m, between 6–7 s.

Figure 15b shows the maximum angular displacement matrix of the cylinder. The angles are seen to range between 0.038 and 2.56 rad and the maximum angle significantly increases compared to the rest of the values. Therefore, it can be inferred that it is close to resonance at $T = 6$–7 s and $H = 4$–4.5 m.

Figure 15c shows the maximum angular displacement matrix for the proposed geometry. This figure shows that the values range between 0.026–2.18 rad, with the largest angle close to the resonance between $H = 4$–4.5 m and $T = 5$–6 s. Furthermore, by comparing the results for the three floats, that with the greatest angular movement is the cylinder with 0.148 rad, followed by the proposed design with 4.7% less, and finally the semi-spheres with a difference of 0.015 rad.
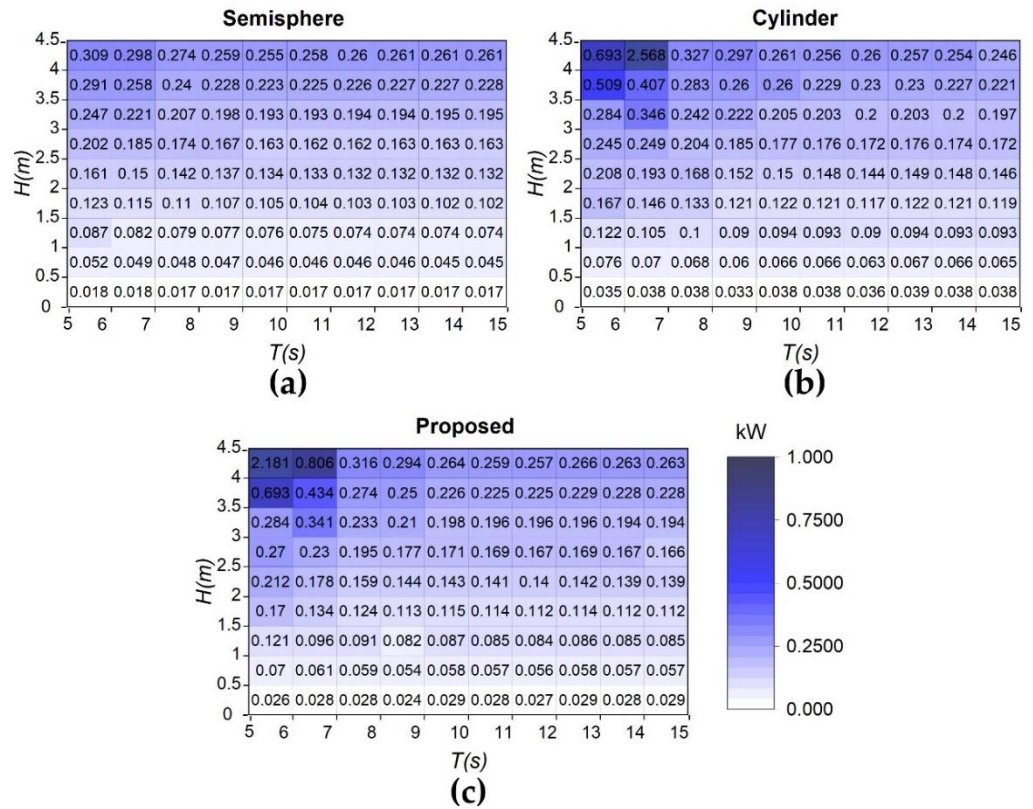
Figure 15. Maximum angular displacement matrix for $T = 5$–15 s with wave heights $H = 0$–4.5 m for (**a**) the semi-sphere, (**b**) the cylinder, and (**c**) the proposed design.

Finally, in Table 5 the maximum angular displacements in each season of the year for the floats obtained from Figure 15 are shown, as well as the annual average of that movement. The cylinder has the greatest displacement in all four seasons of the year, followed by the proposed design, and finally the semi-sphere.

Table 5. Comparison of the average power of the three floats in distinct seasons.

			Semi Sphere	Cylinder	Proposed
Season	H (m)	T (s)	Maximum Angular Displacement (rad)		
Spring	1.97	9.47	0.105	0.122	0.115
Summer	1.51	9.41	0.105	0.122	0.115
Autunm	2.08	10.58	0.133	0.148	0.143
Winter	2.4	11.03	0.132	0.144	0.141
	Average		0.11875	0.134	0.1285

It can also be observed that autumn is when the maximum values occur for the three floats, with values of 0.148, 0.143, and 0.133 rad, respectively. Regarding the annual average values, there are differences between the cylinder, the semi-sphere, and the proposed design of 12.84% and 8.21%, respectively.

Knowing these displacement values helps when selecting the best electric generator, as we then know at what revolutions it must function.

4. Conclusions

The research conducted off the coast of Ensenada, Baja California, Mexico, into the efficiency of three float designs for a PA-WEC highlights the significance of innovative design in improving the performance of renewable energy technologies. The novel geometry introduced in this study—distinct from the usual semi-sphere and cylinder shapes—demonstrates a clear advantage in energy capture efficiency. This innovative design outperformed the more commonly used shapes by substantial margins, 12.6% more efficient than the semi-sphere and 6.7% more than the cylinder, underlining the potential of tailored geometries to optimize wave absorption.

The methodology used in the study, involving analyses both in the frequency and time domains, provides a comprehensive understanding of how these geometries perform in various sea conditions. This type of approach is crucial for identifying designs that can withstand the dynamic, often unpredictable, nature of ocean waves. The frequency domain analysis, focusing on primary forces like added mass, excitation force, radiation damping, and Response Amplitude Operators (RAO), showed that shorter wave periods are more favorable for energy collection regardless of the float shape tested. This insight is particularly valuable for regions like Ensenada, where variable wave patterns can significantly impact the efficiency of WEC systems.

In the time domain evaluation, the proposed design again was seen as the most suitable for the oscillatory movement of waves, a common challenge in wave energy conversion. The ability of the new PTO system to disengage at lower speeds and allow the flywheel to continue spinning, using stored energy, ensures a more stable and consistent energy output. This is one of the key challenges in wave energy conversion.

Seasonal variations in energy capture, with the highest potential being in autumn, followed by winter, spring, and summer, underscores the importance of considering temporal factors in the planning and deployment of WECs. The estimated annual energy output—135.11 MWh for the new design, as opposed to 132.52 MWh and 134.83 MWh for the cylinder and semi-sphere, respectively—reinforces the superiority of the proposed design. Although this difference is seemingly modest, it can significantly impact the long-term viability and economic feasibility of wave energy projects.

In conclusion, this study not only proves the efficacy of the energy capture of the proposed float in a WEC design but also emphasizes the critical role of site-specific analyses and innovative engineering in the field of marine renewable energy. The findings offer promising directions for future research and practical applications, particularly in regions with similar marine conditions to Ensenada, paving the way for more efficient, reliable, and sustainable wave energy conversion solutions.

Author Contributions: Conceptualization, A.M.F. and A.A.M.R.; methodology, A.M.F.; software, A.M.F. and R.S.; validation, A.M.F., E.M. and R.S.; formal analysis, A.M.F., A.A.M.R., E.M. and R.S.; investigation, A.M.F., A.A.M.R. and R.S.; writing—original draft preparation A.M.F. and A.A.M.R.; writing—review and editing A.M.F., A.A.M.R., R.S. and E.M. All authors have read and agreed to the published version of the manuscript.

Data Availability Statement: The data used in the works is available upon request.

Appendix A
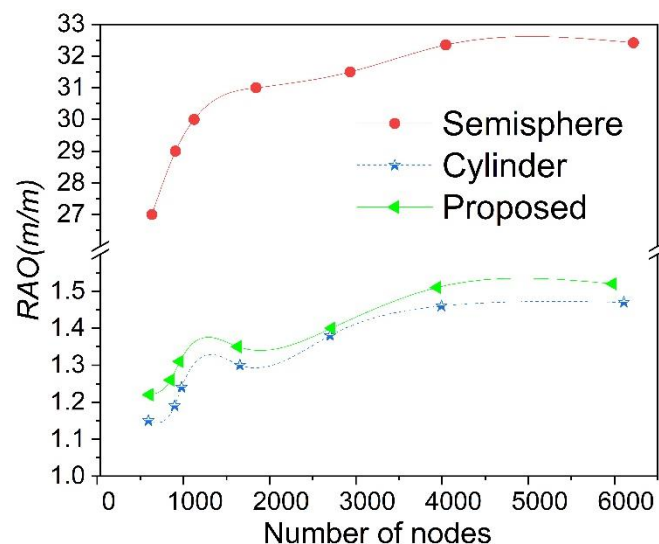
Figure A1. Mesh independence study for the three figures analyzed for RAO in heave.

References

1. Falkner, R. The Paris Agreement and the new logic of international climate politics. *Int. Aff.* **2016**, *92*, 1107–1125. [CrossRef]
2. Poullikkas, A. Technology prospects of wave power systems. *Electron. J. Energy Environ.* **2014**, *2*, 47–69.
3. Hernández-Fontes, J.V.; Felix, A.; Mendoza, E.; Cueto, Y.R.; Silva, R. On the marine energy resources of Mexico. *J. Mar. Sci. Eng.* **2019**, *7*, 191. [CrossRef]
4. Quitoras, M.R.D.; Abundo, M.L.S.; Danao, L.A.M. A techno-economic assessment of wave energy resources in the Philippines. *Renew. Sustain. Energy Rev.* **2018**, *88*, 68–81. [CrossRef]
5. Neill, S.P.; Hashemi, M.R. *Fundamentals of Ocean Renewable Energy: Generating Electricity from the Sea*; Academic Press: Cambridge, MA, USA, 2018.
6. Mork, G.; Barstow, S.; Kabuth, A.; Pontes, M.T. Assessing the global wave energy potential. In Proceedings of the International Conference on Offshore Mechanics and Arctic Engineering, Shanghai, China, 6–11 June 2010; pp. 447–454.
7. Ilyas, A.; Kashif, S.A.; Saqib, M.A.; Asad, M.M. Wave electrical energy systems: Implementation, challenges and environmental issues. *Renew. Sustain. Energy Rev.* **2014**, *40*, 260–268. [CrossRef]
8. Jacobson, P.T.; Hagerman, G.; Scott, G. *Mapping and Assessment of the United States Ocean Wave Energy Resource*; Electric Power Research Institute: Palo Alto, CA, USA, 2011.
9. Kempener, R.; Neumann, F. *Tidal Energy Technology Brief*; International Renewable Energy Agency (IRENA): Masdar City, Abu Dhabi, 2014; pp. 1–34.
10. Sannasiraj, S.; Sundar, V. Assessment of wave energy potential and its harvesting approach along the Indian coast. *Renew. Energy* **2016**, *99*, 398–409. [CrossRef]
11. Gleizon, P.; Campuzano, F.; Carracedo, P.; Martinez, A.; Goggins, J.; Atan, R.; Nash, S. Wave energy resources along the European Atlantic coast. In *Marine Renewable Energy*; Springer: Berlin/Heidelberg, Germany, 2017; pp. 37–69.
12. Cornett, A.M. A global wave energy resource assessment. In Proceedings of the Eighteenth International Offshore and Polar Engineering Conference, Vancouver, BC, Canada, 6–11 July 2008.
13. Mustapa, M.A.; Yaakob, O.; Ahmed, Y.M.; Rheem, C.-K.; Koh, K.; Adnan, F.A. Wave energy device and breakwater integration: A review. *Renew. Sustain. Energy Rev.* **2017**, *77*, 43–58. [CrossRef]
14. López, I.; Andreu, J.; Ceballos, S.; De Alegría, I.M.; Kortabarria, I. Review of wave energy technologies and the necessary power-equipment. *Renew. Sustain. Energy Rev.* **2013**, *27*, 413–434. [CrossRef]
15. Folley, M.; Whittaker, T. Analysis of the nearshore wave energy resource. *Renew. Energy* **2009**, *34*, 1709–1715. [CrossRef]
16. Drew, B.; Plummer, A.R.; Sahinkaya, M.N. A review of wave energy converter technology. *Proc. Inst. Mech. Eng. Part A J. Power Energy* **2009**, *223*, 887–902. [CrossRef]
17. Lagoun, M.; Benalia, A.; Benbouzid, M.H. Ocean wave converters: State of the art and current status. In Proceedings of the 2010 IEEE International Energy Conference, Manama, Bahrain, 18–22 December 2010; pp. 636–641.

18. Polinder, H.; Damen, M.; Gardner, F. Design, modelling and test results of the AWS PM linear generator. *Eur. Trans. Electr. Power* **2005**, *15*, 245–256. [CrossRef]

19. Kofoed, J.P.; Frigaard, P.; Friis-Madsen, E.; Sørensen, H.C. Prototype testing of the wave energy converter wave dragon. *Renew. Energy* **2006**, *31*, 181–189. [CrossRef]

20. Chozas, J.F.; Kramer, M.; Sørensen, H.; Kofoed, J.P. Combined Production of a Full-Scale Wave Converter and a Full-Scale Wind Turbine: A Real Case Study. In Proceedings of the 4th International Conference on Ocean Energy, Dublin, Ireland, 17–19 October 2012.

21. Brito-Melo, A.; Gato, L.; Sarmento, A. Analysis of Wells turbine design parameters by numerical simulation of the OWC performance. *Ocean Eng.* **2002**, *29*, 1463–1477. [CrossRef]

22. Henderson, R. Design, simulation, and testing of a novel hydraulic power take-off system for the Pelamis wave energy converter. *Renew. Energy* **2006**, *31*, 271–283. [CrossRef]

23. Polinder, H.; Damen, M.E.; Gardner, F. Linear PM generator system for wave energy conversion in the AWS. *IEEE Trans. Energy Convers.* **2004**, *19*, 583–589. [CrossRef]

24. Albert, A.; Berselli, G.; Bruzzone, L.; Fanghella, P. Mechanical design and simulation of an onshore four-bar wave energy converter. *Renew. Energy* **2017**, *114*, 766–774. [CrossRef]

25. Heath, T.; Whittaker, T.J.; Boake, C. The Design, Construction and Operation of the LIMPET Wave Energy Converter (Islay, Scotland)[Land Installed Marine Powered Energy Transformer]. 2001. Available online: https://www.osti.gov/etdeweb/biblio/20243723 (accessed on 15 June 2023).

26. Takahashi, S.; Nakada, H.; Ohneda, H.; Shikamori, M. Wave power conversion by a prototype wave power extracting caisson in Sakata port. In *Coastal Engineering 1992*; American Society of Civil Engineers: Reston, VA, USA, 1993; pp. 3440–3453.

27. Arena, F.; Romolo, A.; Malara, G.; Fiamma, V.; Laface, V. The first full operative U-OWC plants in the port of Civitavecchia. In Proceedings of the International Conference on Offshore Mechanics and Arctic Engineering, Trondheim, Norway, 25–30 June 2017; p. V010T009A022.

28. Torre-Enciso, Y.; Ortubia, I.; De Aguileta, L.L.; Marqués, J. Mutriku wave power plant: From the thinking out to the reality. In Proceedings of the 8th European Wave and Tidal Energy Conference, Uppsala, Sweden, 7–10 September 2009; pp. 319–329.

29. Wu, B.; Chen, T.; Jiang, J.; Li, G.; Zhang, Y.; Ye, Y. Economic assessment of wave power boat based on the performance of "Mighty Whale" and BBDB. *Renew. Sustain. Energy Rev.* **2018**, *81*, 946–953. [CrossRef]

30. Whittaker, T.; Collier, D.; Folley, M.; Osterried, M.; Henry, A.; Crowley, M. The development of Oyster—A shallow water surging wave energy converter. In Proceedings of the 7th European Wave and Tidal Energy Conference, Porto, Portugal, 11–13 September 2007; pp. 11–14.

31. Tedd, J.; Kofoed, J.P. Measurements of overtopping flow time series on the Wave Dragon, wave energy converter. *Renew. Energy* **2009**, *34*, 711–717. [CrossRef]

32. Falcão, A.F.; Cândido, J.J.; Justino, P.A.; Henriques, J.C. Hydrodynamics of the IPS buoy wave energy converter including the effect of non-uniform acceleration tube cross section. *Renew. Energy* **2012**, *41*, 105–114. [CrossRef]

33. Wacher, A.; Nielsen, K. Mathematical and numerical modeling of the AquaBuOY wave energy converter. *Math.-In-Ind. Case Stud.* **2010**, *2*, 16–33.

34. Dalton, G.J.; Alcorn, R.; Lewis, T. Case study feasibility analysis of the Pelamis wave energy convertor in Ireland, Portugal and North America. *Renew. Energy* **2010**, *35*, 443–455. [CrossRef]

35. Ruellan, M.; BenAhmed, H.; Multon, B.; Josset, C.; Babarit, A.; Clement, A. Design methodology for a SEAREV wave energy converter. *IEEE Trans. Energy Convers.* **2010**, *25*, 760–767. [CrossRef]

36. Wu, F.; Zhang, X.P.; Ju, P.; Sterling, M.J. Optimal control for AWS-based wave energy conversion system. *IEEE Trans. Power Syst.* **2009**, *24*, 1747–1755.

37. Cameron, L.; Doherty, R.; Henry, A.; Doherty, K.; Van't Hoff, J.; Kaye, D.; Naylor, D.; Bourdier, S.; Whittaker, T. Design of the next generation of the Oyster wave energy converter. In Proceedings of the 3rd International Conference on Ocean Energy, Bilbao, Spain, 6 October 2010; p. 1e12.

38. Marquis, L.; Kramer, M.; Frigaard, P. First power production figures from the wave star roshage wave energy converter. In Proceedings of the 3rd International Conference on Ocean Energy (ICOE-2010), Bilbao, Spain, 6–9 October 2010; pp. 1–5.

39. Chatzigiannakou, M.A.; Dolguntseva, I.; Leijon, M. Offshore deployments of wave energy converters by seabased industry AB. *J. Mar. Sci. Eng.* **2017**, *5*, 15. [CrossRef]

40. Weber, J.; Mouwen, F.; Parish, A.; Robertson, D. Wavebob—Research & development network and tools in the context of systems engineering. In Proceedings of the Eighth European Wave and Tidal Energy Conference, Uppsala, Sweden, 7–10 September 2009; pp. 416–420.

41. Weinstein, A.; Fredrikson, G.; Parks, M.; Nielsen, K. AquaBuOY—The offshore wave energy converter numerical modeling and optimization. In Proceedings of the Oceans' 04 MTS/IEEE Techno-Ocean' 04 (IEEE Cat. No. 04CH37600), Kobe, Japan, 9–12 November 2004; pp. 1854–1859.

42. Budal, K.; Falnes, J. Wave power conversion by point absorbers: A Norwegian project. *Int. J. Ambient Energy* **1982**, *3*, 59–67. [CrossRef]

43. Goggins, J.; Finnegan, W. Shape optimisation of floating wave energy converters for a specified wave energy spectrum. *Renew. Energy* **2014**, *71*, 208–220. [CrossRef]

44. Shi, H.; Han, Z.; Zhao, C. Numerical study on the optimization design of the conical bottom heaving buoy convertor. *Ocean Eng.* **2019**, *173*, 235–243. [CrossRef]

45. McCabe, A. Constrained optimization of the shape of a wave energy collector by genetic algorithm. *Renew. Energy* **2013**, *51*, 274–284. [CrossRef]

46. Shadman, M.; Estefen, S.F.; Rodriguez, C.A.; Nogueira, I.C. A geometrical optimization method applied to a heaving point absorber wave energy converter. *Renew. Energy* **2018**, *115*, 533–546. [CrossRef]

47. Huang, Y.; Xiao, Q.; Idarraga, G.; Yang, L.; Dai, S.; Abad, F.; Brennan, F.; Lotfian, S. Novel computational fluid dynamics-finite element analysis solution for the study of flexible material wave energy converters. *Phys. Fluids* **2023**, *35*, 083611. [CrossRef]

48. Devolder, B.; Stratigaki, V.; Troch, P.; Rauwoens, P. CFD Simulations of Floating Point Absorber Wave Energy Converter Arrays Subjected to Regular Waves. *Energies* **2018**, *11*, 641. [CrossRef]

49. Zhang, D.; Zhao, B.; Jiang, H. Wave energy converter with floating-point absorber and catenary mooring: Dynamic coupling analysis. *Front. Mar. Sci.* **2024**, *11*, 1–19. [CrossRef]

50. Zou, S.; Abdelkhalik, O. A Numerical Simulation of a Variable-Shape Buoy Wave Energy Converter. *J. Mar. Sci. Eng.* **2021**, *9*, 625. [CrossRef]

51. Huang, Q.; Wang, P.; Liu, Y.; Li, B. Modeling and Simulation of Hydraulic Power Take-Off Based on AQWA. *Energies* **2022**, *15*, 3918. [CrossRef]

52. Pastor, J.; Liu, Y. Power Absorption Modeling and Optimization of a Point Absorbing Wave Energy Converter Using Numerical Method. *J. Energy Resour. Technol.* **2014**, *136*, 021207. [CrossRef]

53. Falnes, J.; Perlin, M. Ocean waves and oscillating systems: Linear interactions including wave-energy extraction. *J. Appl. Mech. Rev.* **2003**, *56*, B3. [CrossRef]

54. Hagerman, G. Southern New England wave energy resource potential. In Proceedings of the Building Energy, Boston, MA, USA, 21–24 March 2001.

55. Newman, J.N. *Marine Hydrodynamics*; The MIT Press: Cambridge, MA, USA, 2018.

56. ANSYS. *ANSYS AQWA Theory Manual, Release 18.2*; ANSYS: Canonsburg, PA, USA, 2017.

57. Silva, R.; Mendoza, E.; Losada, M.A. Modelling linear wave transformation induced by dissipative structures—Regular waves. *Ocean Eng.* **2006**, *33*, 2150–2173. [CrossRef]

58. Mendoza, E.; Silva, R.; Zanuttigh, B.; Angelelli, E.; Lykke Andersen, T.; Martinelli, L.; Nørgaard, J.Q.H.; Ruol, P. Beach response to wave energy converter farms acting as coastal defence. *Coast. Eng.* **2014**, *87*, 97–111. [CrossRef]

59. Silva, R.; Baquerizo, A.; Losada, M.Á.; Mendoza, E. Hydrodynamics of a headland-bay beach—Nearshore current circulation. *Coast. Eng.* **2010**, *57*, 160–175. [CrossRef]

60. Silva, R.; Borthwick, A.G.L.; Taylor, R.E. Numerical implementation of the harmonic modified mild-slope equation. *Coast. Eng.* **2005**, *52*, 391–407. [CrossRef]

61. Polinder, H.; Scuotto, M. Wave energy converters and their impact on power systems. In Proceedings of the 2005 International Conference on Future Power Systems, Amsterdam, The Netherlands, 18 November 2005; p. 9.

62. Dean, R.G.; Dalrymple, R.A. *Water Wave Mechanics for Engineers and Scientists*; World Scientific Publishing Company: Singapore, 1991; Volume 2.

63. Alejandro, M.F.; Israel, H.H.J.; Ayrton, M.R.; Medina, M.B.E.G.; Rodolfo, S.C. Dinámica de una caja de velocidad unidireccional para un convertidor de energía undimotriz. In Proceedings of the Congreso Internacional Anual de la SOMIM, Mazatlán, Mexico; 2019.